Effect of Surface Microgeometry on Deformation and Stresses in Elastic-Plastic Layered Media

Z.-Q. Gong, Graduate Student
K. Komvopoulos, Professor, Fellow ASME

Department of Mechanical Engineering
University of California
Berkeley, CA 94720

Abstract

Plane-strain normal contact and sliding of a rigid asperity on an elastic-plastic layered medium with a patterned surface was investigated using the finite element method in order to obtain insight into the effect of the surface microgeometry (patterning) on the resulting deformation and stresses in the medium. Interaction of the moving asperity with the deformable medium was modeled by contact elements. Simulations were performed for meandered and sinusoidal surface patterns with different geometric parameters. Results for the contact pressure distribution, surface tensile stress, and subsurface plastic strain are presented for each surface pattern. The significance of surface microgeometry parameters on the maximum contact pressure and von Mises equivalent stress in the surface layer is examined in terms of the normal load. Relations for the pressure concentration factor and a general yield criterion for layered media with sinusoidal surfaces are derived from finite element results. Good agreement was found between predictions for the critical indentation depth at the inception of plasticity obtained from the yield criterion and finite element simulations.

Submitted to the ASME *Journal of Tribology* on January 15, 2002.

1. Introduction

Surface coatings are often used to protect components subjected to contact stresses and to enhance the tribological performance and functional lifetime of interacting surfaces. Numerous theoretical and numerical analyses of elastic-plastic layered media subjected to indentation and sliding contact have been presented over the past two decades. A major common objective has been the study of the effect of the thickness and mechanical properties of the overcoat on the resulting contact stress and deformation fields. In the majority of these studies, the indenting or sliding asperity was assumed to interact with a layered medium with a flat surface. Thus, very little is known about the role of surface microgeometry features on the elastic-plastic deformation and stresses in layered media.

Contact of elastic bodies with small-amplitude sinusoidal surfaces has been the main objective in several early studies dealing with the influence of surface geometry on contact stresses. Westergaard (1939) used complex variables in two-dimensional elasticity to analyze contact of a sinusoidal surface with a flat surface. Dundurs et al. (1973) obtained solutions for the previous contact problem by implementing a Fourier analysis in a stress function approach. A theoretical treatment to the contact problem of two elastic half-spaces having a two-dimensional sinusoidal isotropic wavy surface with amplitude smaller than its wavelength is cumbersome. Experimental results have shown that it is not possible to predict the shape of microcontact areas (Johnson et al., 1985). As the normal load increases, the shapes of microcontacts in the apparent contact region change from approximately circular to squared, resulting eventually in real contact areas containing small circular noncontacting regions. Johnson et al. (1985) used a numerical method to determine the pressure distribution and contact area, and developed closed-form asymptotic solutions for both light and heavy loads at which almost full contact was found

to occur. Seabra and Berthe (1987) used a variational formulation to study normal contact of an infinitely long wavy cylinder with a flat plane and reported that both the pressure concentration factor and the change of the contact area were strong functions of wavelength, amplitude, and load. It was also shown that the effect of surface roughness on the contact behavior was qualitatively identical to that of the surface waviness. Ramachandra and Ovaert (2001) performed a numerical study of the effect of coating discontinuities on the elastic surface stresses and showed a significant decrease of pressure singularities at the boundaries of coating discontinuities with crowned edges.

Although the previous analyses have yielded useful insight into the significance of surface geometry on contact deformation of homogeneous media, very little is known about the elastic-plastic deformation and stresses arising in layered media with patterned surfaces due to normal and tangential (friction) surface traction. Therefore, the main objective of this study was to elucidate the coupled effects of surface microgeometry, coefficient of friction, and normal load (or penetration depth) on the evolution of deformation and stress in elastic-plastic layered media in light of finite element simulations of normal and sliding contact with a rigid cylindrical asperity. Another goal of this work was to derive relations for the contact pressure concentration factor and inception of yielding due to indentation of layered media possessing sinusoidal surface patterns.

2. Modeling Procedures

2.1 Surface Modeling and Finite Element Mesh

To examine the effect of surface microgeometry on the deformation and stresses in elastic-plastic layered media, meandered surfaces consisting of bit cells of height b and width and lateral spacing a (Fig. 1(a)) and sinusoidal surfaces of wavelength λ and amplitude δ (Fig. 1(b)) were

used in finite element contact simulations. Different surface patterns were modeled by varying the dimensionless ratios b/a and δ/λ. The radius of the rigid asperity R was fixed at 200 nm.

Normal contact and sliding simulations were performed with the two-dimensional finite element mesh shown in Fig. 2, based on the usual plane strain assumption. The mesh consists of approximately 10,000 eight-node isoparametric quadrilateral elements, depending on the modeled surface pattern, and its dimensions are $x/R = 2.4$ and $y/R = 3.1$. The nodes at the bottom boundary of the mesh were constrained against displacement in the y-direction, while the nodes at the left boundary of the mesh were constrained against displacement in both x- and y-directions. To accurately determine the contact pressure distribution, contact area, and stress and strain fields in the highly stressed region adjacent to the contact interface, small square elements of sides equal to 1/32 of the first layer thickness were used to refine the mesh near the surface, as shown in Fig. 2(a) for a layered medium having a sinusoidal surface microgeometry. A 3 x 3 integration scheme was used in all simulations. Special contact elements were used to detect contact between the surface of the deformable medium and the rigid asperity. With these elements, contact or separation between surface nodal points and the rigid surface is determined by measuring the local gap between the two surfaces. If the obtained distance is less than a specified tolerance value, it is assumed that contact is established and appropriate force (contact pressure) is applied at associated surface nodes of the mesh. A measure of the local overclosure, i.e., the penetration of a point on the surface of the deformable body into the rigid surface, is also obtained from the contact elements and used to determine relative sliding. These kinematic measures are used together with a Lagrange multiplier to model surface interaction due to normal and friction traction.

2.2 Material Properties and Constitutive Models

The thickness h, elastic modulus E, and yield strength σ_Y of each layer of the deformable medium are given in Table 1. These thickness and material property values are typical of those of layers in magnetic recording rigid disks, i.e., carbon overcoat (layer 1), CoCrPt magnetic medium (layer 2), CrV underlayer (layer 3), and NiP electroplated layer (layer 4). The material properties of layers 1 and 2 were obtained from nanoindentation measurements (Komvopoulos, 2000).

The von Mises yield criterion was used to determine whether yielding occurred at a material point. According to this criterion, the yield condition g can be expressed as

$$g = J_2 - k^2 = 0, \tag{1}$$

where k is a material constant and J_2 is the second deviatoric stress invariant, given by

$$J_2 = \frac{1}{2} S_{ij} S_{ij}, \tag{2}$$

where $S_{ij} = \sigma_{ij} - \delta_{ij}\sigma_m$, in which σ_{ij} is the stress tensor, δ_{ij} is Kronecker's delta function, and σ_m is the mean octahedral stress given by $\sigma_m = \sigma_{\mathrm{ii}}/3$.

For a uniaxial stress state, the yield criterion can be written as

$$\sigma_M = \left[\frac{3}{2} S_{ij} S_{ij} \right]^{1/2} = \sigma_Y \tag{3}$$

where σ_M is the von Mises equivalent stress and σ_Y is the uniaxial tensile yield stress. Plastic deformation is based on the usual associated flow rule, assuming negligible plastic volume change. An updated Lagrangian formulation was used in the present analysis. All layers were assumed to exhibit elastic-perfectly plastic material behavior. The equivalent plastic strain $\bar{\varepsilon}_p$ is defined as

$$\bar{\varepsilon}_p = \int_\Gamma \sqrt{\frac{2}{3} d\varepsilon_{ij}^p d\varepsilon_{ij}^p} \tag{4}$$

where Γ is the strain path. The plastic flow rule is applied only to yielding material for which $\sigma_M = \sigma_Y$. The usual elastic constitutive equations are used when $\sigma_M < \sigma_Y$.

2.3 Finite Element Simulations

Quasi-static contact simulations comprising three sequential steps of loading, sliding, and unloading of a rigid asperity on layered media with different surface microgeometries were performed in an incremental fashion. Normal contact (indentation) was simulated by advancing the rigid asperity toward the elastic-plastic medium up to a specified penetration depth d (or normal load). Then the asperity was displaced laterally to a specified total distance S of about eight times the contact width at maximum normal load. During sliding, the coefficient of friction μ and normal load L were maintained constant. Finally, the asperity was unloaded following the same steps as for the loading. All simulations were performed with the multipurpose finite element code ABAQUS. A total of 12 simulation cases were examined (i.e., eight sliding and four normal contact cases), i.e., b/a = 0.0, 0.5, 1, and 2 (meandered surfaces, Table 2) and δ/λ = 0, 0.008, 0.016, and 0.032 (sinusoidal surfaces, Table 3). The friction coefficient values of 0.1 and 0.5 may be considered to be representative of boundary-lubricated and dry or poorly lubricated surfaces, respectively.

3. Results and Discussion

To elucidate the effect of the surface microgeometry on the contact deformation behavior, elastic-plastic finite element results for the surface and subsurface stresses and strains in layered media with meandered and sinusoidal surfaces in sliding contact with a rigid asperity are

presented in this section. For the geometry, material, and load parameters considered in this study, deformation was found to occur mainly in the first two layers. Thus, results illustrating the evolution of stress and deformation in layers 1 and 2 are presented first, followed by an analysis for the contact pressure concentration factor and a general yield criterion for indented layered media with sinusoidal surfaces.

3.1 Sliding Contact Simulations

3.1.1 Contact Pressure

Figures 3 and 4 show contact pressure distributions on layered media possessing meandered and sinusoidal surface patterns for sliding distance S/R = 0.125 nm, dimensionless normal load $L/\sigma_{Y1}a_0$ = 0.57, and different values of topography parameters b/a and δ/λ, respectively. The normal load is normalized by the contact width a_0 and the contact pressure p by the maximum contact pressure $p_0^{\max}$ corresponding to a layered medium with a flat surface and similar layer thickness and material properties subjected to identical loading conditions. The contact pressure of this layered medium is also plotted in Fig. 3 (a/b = 0) and Fig. 4 (δ/λ = 0) for comparison. The pressure profiles of the patterned media are distinctly different from those of the flat-surface medium. Five microcontact regions with peak pressures occurring at the trailing edges (with respect to the sliding direction of the asperity) of the meandered patterns (referred to as "bit cells") can be seen in Fig. 3. These local pressure spikes are evidently due to stress concentration effects. Comparison of Figs. 3(a)-3(c) shows that the magnitudes of the peak pressures increases significantly with the ratio b/a.

The effect of surface roughening on the contact pressure distribution can be interpreted by comparing the pressure profiles for δ/λ = 0.008, 0.016, and 0.032 and identical normal load and coefficient of friction (Fig. 4). For the relatively rougher surfaces, i.e., δ/λ = 0.016 (Fig. 4(b))

and δ/λ = 0.032 (Fig. 4(c)), five distinct microcontact regions were established, similar to the layered media with meandered surfaces (Fig. 3). However, for the low-roughness simulation case δ/λ = 0.008 (Fig. 4(a)), the contact pressure is lower and varies less abruptly. In addition, the continuity of the pressure profile at the center of the contact reveals the merger of the three microcontacts in this region of the interface. A similar behavior was observed in a previous contact analysis of two-dimensional discontinuous coatings (Ramachandra and Ovaert, 2000). As shown in Fig. 4, the contact pressure distribution and maximum contact pressure are very sensitive to the surface roughness, and the peak contact pressure increases rapidly with the δ/λ ratio.

3.1.2 Surface Stresses

The von Mises equivalent stress is often used to analyze material failure. However, it is not possible to differentiate between failures associated with predominantly compressive and tensile stress states based on the von Mises yield criterion. Hard materials exhibit a much higher resistance to inelastic deformation under compression than tension because the high material hardness (or yield strength) is obtained at the expense of low fracture toughness. Consequently, fracture and delamination of hard and stiff protective coatings becomes the dominant failure mechanisms in many tribological contacts. The susceptibility to cracking and the integrity of a coating depends on the magnitude of the maximum tensile stress, such as the surface normal stress σ_{xx}. Figure 5 shows the evolution of σ_{xx} stress on the surface of layered media possessing "smooth" (δ/λ = 0) and "rough" (δ/λ = 0.008, 0.016, and 0.032) surfaces with sliding for μ = 0.5. (Stress results in Fig. 5, as well as in subsequent figures, are normalized by the yield strength of the first layer σ_Y). Four regions of tensile stress are encountered at the sliding interface of the media with rough surfaces, and significantly higher tensile stresses arise at the trailing edges of

microcontacts at the contact interfaces of the rough (sinusoidal) surfaces, conversely to the smooth (flat) surface which demonstrates a continuous compressive stress distribution. The magnitude of the peak tensile σ_{xx} stress increases with the ratio δ/λ, indicating that rougher surfaces yield higher surface tensile stresses. For the rougher surface (δ/λ = 0.032), the maximum tensile σ_{xx} stress at the contact interface is very close to the yield strength of the layer material. Moreover, the significant residual tensile stress in the wake of the sliding path obtained in the simulation case of δ/λ = 0.032 supports the view that rough surfaces are more vulnerable to contact fatigue due to repetitive sliding.

Since the surface σ_{xx} stress is the first principal stress in the layer medium, it is responsible for the initiation of transverse (ring) surface cracks in the wake of sliding microcontacts, a phenomenon often encountered when sliding rigid indenters on brittle materials. Formation of ring cracks on carbon-coated rigid disks was observed in scratching experiments (Wu, 1991). This type of surface cracking has been the objective of several contact mechanics analyses (Keer and Worden, 1990); Keer and Kuo, 1992; Chen et al., 1991; Bower and Fleck, 1994). Results from these studies have confirmed that surface crack initiation at surfaces of homogeneous media commences immediately behind the contact region of the sliding indenter, where the tensile stress reaches a maximum.

To evaluate the effect of friction on the propensity of a layered medium for surface cracking, the stress results shown in Fig. 5 (μ = 0.5) are compared with those shown in Fig. 6 (μ = 0.1). The low-friction simulation results reveal a similar trend, i.e., peak tensile stresses arise at the trailing edges of microcontacts at the sliding interface. However, the magnitudes of the maximum tensile stresses are significantly lower than those obtained for μ = 0.5, and the residual stress at the wake of the sliding path is negligibly small, similar to that obtained with the flat-

surface layered medium. This suggests that the effect of surface roughness on plastic deformation (reflected by the development of residual stress) is suppressed when friction at the sliding interface is low, such as in boundary-lubricated surfaces, even in the case of relatively rough surface topographies (i.e., high δ/λ values).

To further elucidate the effect of surface texture (roughness) on the maximum tensile stress at the surface, results for the maximum first principal stress in the first layer σ_1^{max} (which is the surface tensile σ_{xx} stress at the wake of the sliding asperity) versus sliding distance S/R for δ/λ between 0 and 0.032 and $\mu = 0.5$ are contrasted in Fig. 7. In all simulation cases, the maximum tensile stress increases rapidly with the initiation of sliding, reaching a steady state at a sliding distance of $S/R = 0.125$, which is in agreement with the prediction of a previous finite element analysis (Kral and Komvopoulos, 1996). Increasing the roughness parameter δ/λ causes the maximum tensile stress in the first layer to increase significantly. For $\delta/\lambda = 0.032$, this stress is close to the yield strength of the layer. As shown in Fig. 7(b), tensile stresses occur also in the second layer. (The stress results are normalized by the yield strength of the second layer σ_{Y2}.) While the surface texture effect is negligible in the initial stage of sliding ($S/R < 0.2$), a trend similar to that observed for the first layer is observed thereafter, i.e., the maximum first principal stress assumes higher values as δ/λ increases, reaching a steady-state value at $S/R > 0.25$. However, comparison of the results shown in Figs. 7(a) and 7(b) shows that maximum tensile stress in the second layer is significantly lower than that at the surface. Thus, the harder surface layer protects the underlying softer layer from the high tensile surface stresses that would have had otherwise occurred under direct sliding contact, thus decreasing the likelihood of crack initiation and damage in the second layer.

3.1.3 Evolution of Plasticity in Layered Media

To examine the dependence of plasticity on sliding friction, equivalent plastic strain $\bar{\varepsilon}_p$ contours for $\mu = 0.5$ and 0.1, $\delta/\lambda = 0.032$, and $S/R = 0.5$ are contrasted in Fig. 8. For relatively high friction ($\mu = 0.5$), a continuous plastic zone is produced in the second layer, with the maximum plastic strain occurring at the interface with the first layer, where plasticity manifests itself in the form of very small localized plastic zones at the sliding surface (Fig. 8(a)). For low-friction sliding conditions ($\mu = 0.1$), a discontinuous plastic zone exhibiting periodicity similar to that of the surface waviness evolves in the second layer (Fig. 8(b)). However, the maximum plastic strain is much lower than that in the high-friction case and the first layer deforms only elastically. These results demonstrate the pronounced effect of tangential (friction) traction at stress raiser points of the surface on the development of subsurface plasticity in the layered medium. Similar trends were observed for different values of δ/λ.

Figures 9(a) and 9(b) show the maximum equivalent plastic strain $\bar{\varepsilon}_p^{\max}$ in the second layer of layered media with meandered and sinusoidal surfaces, respectively, as a function of sliding distance S/R. The continuous decrease of the slopes of all the curves is indicative of the approach to steady-state peak plastic strains in the range of 0.08-0.15. Nonetheless, the most important finding is the decrease of plasticity with increasing b/a and δ/λ. This is more apparent with the sinusoidal surfaces that produced lower plastic strains, a consequence of the less pronounced stress concentration effect due to the absence of sharp corners, contrary to the bit cells of the meandered surfaces. For instance, at $S/R = 0.5$ the maximum plastic strain in the second layer for $\delta/\lambda = 0.032$ is ~60% of that obtained for $\delta/\lambda = 0$. This behavior can be explained in terms of the effect of surface texturing on the compliance of the stiffer first layer. Increasing b/a or δ/λ results in a more compliant layer that can dissipate more strain energy without undergoing plastic deformation. Thus the reduced "effective" stiffness of the first layer produces lower subsurface

stresses, which decreases the likelihood of plastic flow in the second layer. However, as discussed in previous sections, increasing δ/λ enhances the magnitude of the maximum first principal stress at the trailing edge of the contact region, while increasing b/a promotes the development of high pressure spikes, indicating a greater likelihood for surface crack initiation and plastic flow, respectively. Consequently, an optimum range of δ/λ (or b/a) should be determined to minimize the probability for surface cracking and subsurface plastic deformation.

3.2 Normal Contact Simulations

In this section, semi-empirical relations for the contact pressure concentration factor and the inception of yielding in layered media with sinusoidal surfaces are developed based on finite element simulation results for the contact pressure and deformation fields resulting from normal contact (indentation) with a rigid asperity. Material properties and simulation parameters are given in Table 1 and 2, respectively.

3.2.1 Contact Pressure Concentration Factor

The contact pressure profile in the case of indented layered media with sinusoidal surfaces is fairly similar to that for sliding contact (Fig. 4), except that the profile for normal contact is symmetric. The dependence of the contact pressure on surface geometry parameters and indentation depth is of particular interest. The contact pressure concentration factor K_p is defined as the ratio of the maximum contact pressure of the sinusoidal-surface layered medium to that of the flat-surface layered medium. Figure 10 shows the variation of K_p with normalized indentation depth d/R for different values of δ/λ and $\mu = 0.5$. In all cases, K_p decreases monotonically with increasing indentation depth (or normal load) and wavelength and increases with amplitude. This trend is in qualitative agreement with results from a contact analysis of a wavy cylinder and a plane (Seabra and Berthe, 1987).

The finite element results for δ/λ = 0.008 and 0.016 (δ/λ = 0.032 data were not used because plastic deformation occurred in some of these simulations) were used to fit the following relation,

$$K_p = C(\frac{\delta}{\lambda})^{\alpha}(\frac{d}{R})^{\beta} \quad (5)$$

After some iterations, it was found that C = 2.0327, α = 0.4578, and β = -0.1978. The correlation factor for this fit was found to be equal to 0.996. Since the material parameters and layer thickness values used in the finite element simulations for these layered media affect the magnitudes of these parameters, the obtained values of C, α, and β are specific to these media. The same approach can be repeated to obtain best-fit values for other material and thickness values of the layer. Nevertheless, Eq. (5) provides a means for predicting the increase of the contact pressure on layered media due to roughness effects.

3.2.2 Yield Criterion

Figure 11 shows the normalized maximum von Mises equivalent stress in the first layer $\sigma_M^{\max}/\sigma_Y$ of layered media with sinusoidal surfaces as a function of indentation depth. The maximum von Mises equivalent stress increases with increasing roughness parameter δ/λ and indentation depth d/R (or normal load). However, the roughness effect is significantly more pronounced than the normal load effect. For δ/λ = 0.032, $\sigma_M^{\max}$ reaches the yield stress of the first layer at indentation depth d/R = 0.01.

Based on the simulation results for δ/λ = 0.008 and 0.016, a yield criterion for layered media with sinusoidal surfaces was obtained by fitting the following expression to the finite element results

$$\frac{\sigma_M^{max}}{\sigma_y} = C_1(\frac{\delta}{\lambda})^{\gamma}(\frac{d}{R})^{\eta} \le 1 \qquad (6)$$

After an iterative procedure, it was determined that $\gamma = 0.5173$ and $\eta = 0.2715$, while C_1 depends on the material properties. To derive a more general yield criterion, different material properties were used to obtain a relation for C_1. Figure 12 shows the variation of σ_M^{max} in the first layer with indentation depth, d/R, for different values of the ratio of the elastic modulus of the first and second layers E_1/E_2, $\delta/\lambda = 0.016$, and $\mu = 0.5$. It is shown that σ_M^{max} increases with both E_1/E_2 and d/R. After fitting to the finite element results a relation of the form,

$$C_1 = C_2\left[\frac{E_l/(1-\nu_l^2)}{E_s/(1-\nu_s^2)}\right]^m \qquad (7)$$

it was found that $C_2 = 17.1798$ and $m = 0.6935$ (the correlation factor was found to be equal to 0.998). Substituting Eq. (7) into Eq. (6), the following general yield criterion for a layered media with sinusoidal surfaces is obtained

$$\frac{\sigma_M^{max}}{\sigma_y} = C_2\left[\frac{E_l/(1-\nu_l^2)}{E_s/(1-\nu_s^2)}\right]^m (\frac{\delta}{\lambda})^{\gamma}(\frac{d}{R})^{\eta} \le 1 \qquad (8)$$

where γ, η, m, and C_2 are material constants. Based on this yield criterion, the normal load at the inception of yielding can be predicted for given material properties and geometric parameters. To evaluate the accuracy of the yield criterion, the yield loads of layered media with sinusoidal surfaces calculated from Eq. (8) were compared with those determined directly from finite element simulations. Figure 13 shows a comparison between analytical and finite element results. (A comparison for $\delta/\lambda = 0.008$ was not possible due to the excessive computation time of the finite element simulation to the point of yielding.) For $\delta/\lambda = 0.032$, the onset of yielding is predicted by Eq. (8) to commence at $d/R = 0.01$, which is exactly the value obtained from the

finite element analysis. To examine the case of $\delta/\lambda = 0.016$, the asperity radius was reduced by a factor of 4 in order to reduce the indentation depth at yielding (and thus the computation time). As shown in Fig. 13, the inception of yielding is predicted by Eq. (8) to occur at $d/R = 0.038$, whereas the finite element result is $d/R = 0.04$, i.e., the difference between the results of the two methods is 5%.

4. Conclusions

A two-dimensional plane-strain finite element analysis of normal and sliding contact on elastic-plastic layered media was performed in order to elucidate the effect of surface microgeometry (patterning) on the resulting deformation behavior. Stress and plastic strain results for layered media possessing meandered and sinusoidal surface microgeometries were compared with those of a layered medium with a smooth (flat) surface and identical layer thickness and material properties subjected to the same loading history. Based on the presented results and discussion, the following main conclusions can be drawn.

1. The apparent contact areas of layered media possessing patterned surfaces interacting with a rigid cylindrical asperity consist of several microcontacts that tend to merge with each other with increasing indentation depth (or normal load). High peak pressures occur at the trailing edges of the microcontacts, similar to the pressure profile obtained with the flat-surface layered medium. The maximum contact pressure is a strong function of the surface microgeometry, characterized by nondimensional parameters representative of surface features. Significantly higher peak pressures occur at the sharp edges (stress raisers) of bit cells on meandered surfaces. In contrast, the contact pressure at microcontacts within the sliding interface of layered media with sinusoidal surfaces increases smoothly because of the continuity of the surface profile.

2. Surface tensile stresses in the direction of sliding reveal a tendency for transverse (ring) crack initiation at the surface, in the wake of the sliding path. The maximum tensile residual stress on layered media with sinusoidal surfaces occurs at the trailing edge of the contact region. This residual stress is much larger than that of the flat-surface medium and depends on the surface microgeometry (roughness) and friction coefficient. For relatively rough surfaces (i.e., high amplitude-to-wavelength ratio) and high friction, a significant tensile residual stress develops in the wake of the sliding path. This residual tensile stress may continue to increase with the accumulation of sliding cycles leading to surface cracking. Conversely to the flat surface that yields a purely compressive stress field, small regions of tensile stress occur within the contact interface of layered media with sinusoidal surfaces.
3. The maximum plastic strain decreases with the amplitude-to-wavelength ratio during sliding contact. Patterned surfaces exhibit less plasticity than flat surfaces. This is due to the lower stresses stemming from the greater surface compliance of patterned media that can dissipate more strain energy by deforming only elastically. The ramification of the decreased surface stiffness is the reduced plasticity in the underlying softer layer. However, this arises at the expense of a higher surface tensile stress at the trailing edge of the contact interface, indicating a greater probability of surface crack initiation.
4. Relations for the contact pressure concentration factor and inception of yielding in layered media with sinusoidal surface topographies due to normal contact (indentation) were derived from finite element results using a best-fit approach. The contact pressure concentration factor decreases with increasing indentation depth (normal load) and wavelength-to-amplitude ratio. The yield criterion accounts for the effects of material properties, surface microgeometry, and contact load, and is in good agreement with finite element predictions.

Yielding is predominantly controlled by the wavelength-to-amplitude ratio and secondarily by the indentation depth.

Acknowledgments

This work was partially supported by the National Storage Industry Consortium (NSIC), Extremely High Density Recording (EHDR) Program, and the Computer Mechanics Laboratory at the University of California at Berkeley.

References

Bower, A. F., and Fleck, N. A., 1994, "Brittle Fracture under Sliding Line Contact," Journal of Mechanics and Physics of Solids **42**, pp. 1375-1396.

Dundurs, J., Tsai, K. C., and Keer, L. M., 1973, "Contact of Elastic Bodies with Wavy Surfaces," Journal of Elasticity **3**, pp. 109-115.

Chen, L. M., Farris, F. N., and Chandrasekar, S., 1991, "Sliding Microindentation Fracture of Brittle Materials," Tribology Transactions **34**, pp. 161-168.

Johnson, K. L., Greenwood, J. A., and Higginson, J. G., 1985, "The Contact of Elastic Wavy Surfaces," International Journal of Mechanical Sciences **27**, pp. 383-396.

Keer, L. M., and Worden, R. E., 1990, "A Qualitative Model to Describe the Microchipping Wear Mode in Ceramic Rollers," Tribology Transactions **33**, pp. 411-417.

Keer, L. M., and Kuo, C. H., 1992, "Cracking in a Loaded Brittle Elastic Half-space," International Journal of Solids and Structures **29**, pp. 1819-1826.

Komvopoulos, K., 2000, "Head-Disk Interface Contact Mechanics for Ultrahigh Density Magnetic Recording," Wear **238**, pp. 1-11.

Kral, E. R., and Komvopoulos, K., 1996, "Three-Dimensional Finite Element Analysis of Surface Deformation and Stresses in an Elastic-Plastic Layered Medium Subjected to Indentation and Sliding Contact Loading," ASME Journal of Applied Mechanics **63**, pp. 365-375.

Ramachandra, S., and Ovaert, T. C., 2000, "Effect of Coating Geometry on Contact Stresses in Two-Dimensional Discontinuous Coatings," ASME Journal of Tribology **122**, pp. 665-671.

Seabra, J., and Berthe, D., 1987, "Influence of Surface Waviness and Roughness on the Normal Pressure on the Normal Pressure Distribution in the Hertzian Contact," ASME Journal of Tribology **109**, pp. 462-470.

Westergaard, H. M., 1939, "Bearing Pressures and Cracks," ASME Journal of Applied Mechanics **6**, pp. 49-53.

Wu, T. W., 1991, "Microscratch and Load Relaxation Tests for Ultra-thin Films," Journal of Materials Research **6**, pp. 407-426.

Table 1. Thickness and material properties of layered medium

Medium	h (nm)	E (GPa)	σ_Y (GPa)
Layer 1	5	168	13.0
Layer 2	15.6	130	2.67
Layer 3	80	140	2.58
Layer 4	520	160	2.67

Table 2. Contact simulations for layered media with meandered surfaces

b/a	$L/\sigma_{Y1}a_0$	μ	S/R
0.0	0.57	0.1/0.5	0.5
0.5	0.57	0.1/0.5	0.5
1.0	0.57	0.1/0.5	0.5
2.0	0.57	0.1/0.5	0.5

Table 3. Contact simulations for layered media with sinusoidal surfaces

δ/λ	Sliding			Normal contact	
	$L/\sigma_{Y1}a_0$	μ	S/R	d/R	μ
0.0	0.57	0.1/0.5	0.5	0.0025-0.015	0.5
0.008	0.57	0.1/0.5	0.5	0.0025-0.015	0.5
0.016	0.57	0.1/0.5	0.5	0.0025-0.015	0.5
0.032	0.57	0.1/0.5	0.5	0.0025-0.015	0.5

List of Figures

Fig. 11. Maximum von Mises equivalent stress $\sigma_M^{\max}$ in the first layer of layered media with sinusoidal surfaces versus indentation depth d/R ($\mu = 0.5$).

Fig. 12. Maximum von Mises equivalent stress $\sigma_M^{\max}$ in the first layer of layered media with sinusoidal surfaces versus indentation depth d/R and first-to-second layer elastic modulus ratio E_1/E_2 ($\mu = 0.5$).

Fig. 13. Comparison of finite element and analytical results for the maximum von Mises equivalent stress $\sigma_M^{\max}$ in the first layer of layered media with sinusoidal surfaces versus indentation depth d/R ($\mu = 0.5$).

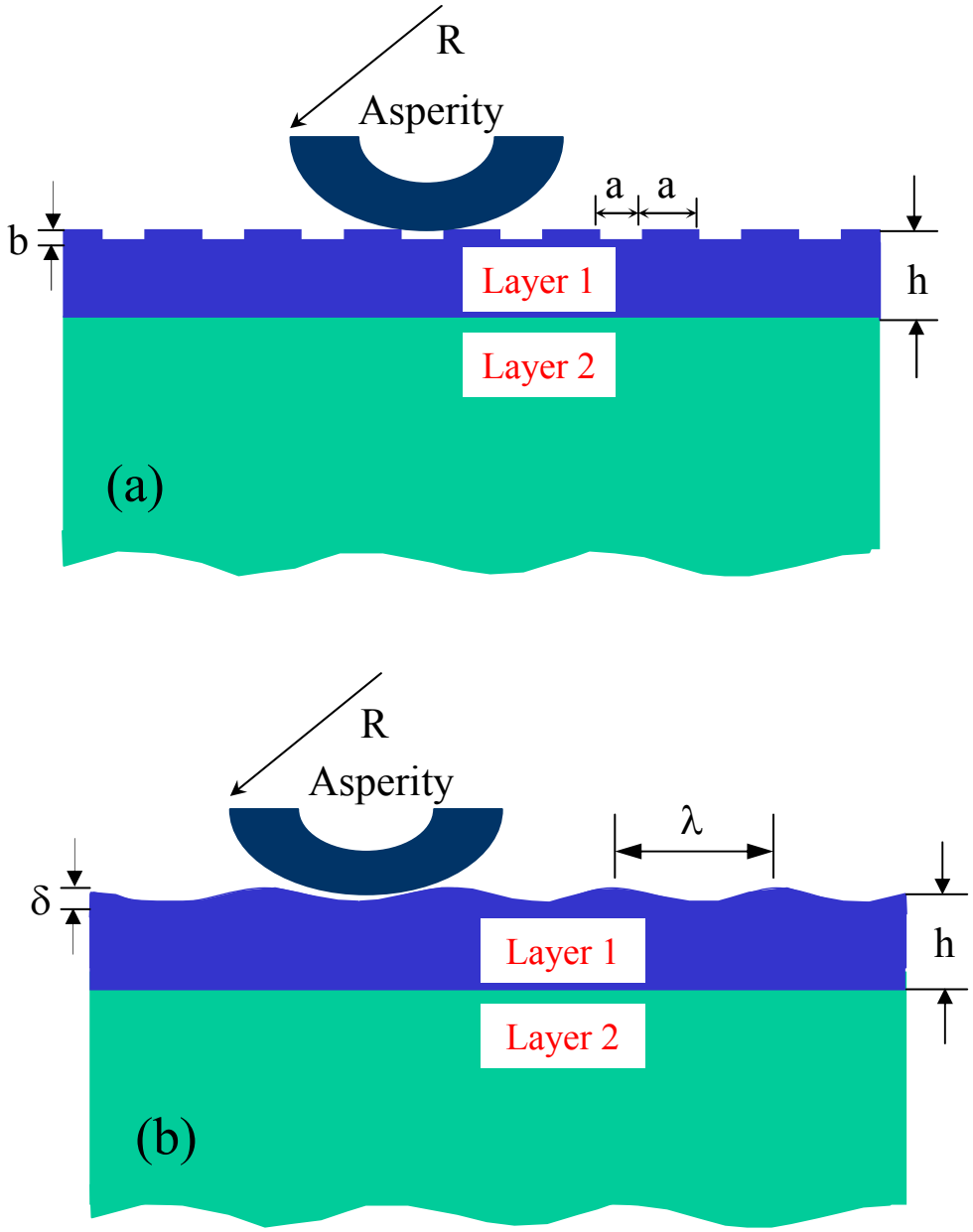
R
Asperity
a
a
b
h
Layer 1
Layer 2
(a)
R
Asperity
λ
δ
h
Layer 1
Layer 2
(b)

Figure 1

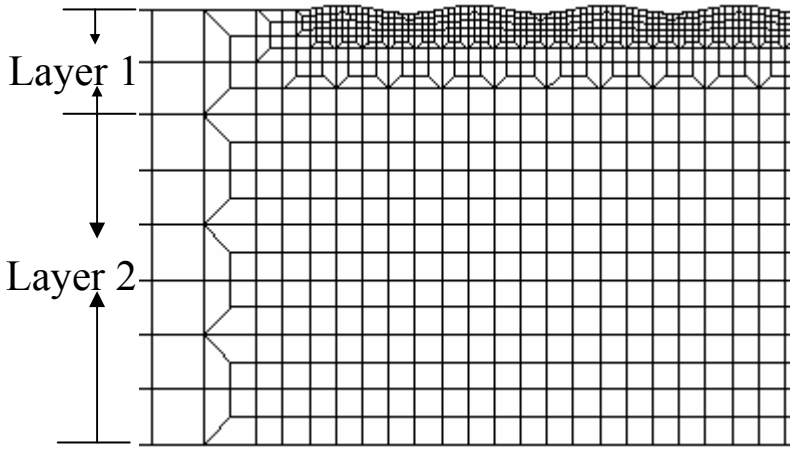

(a)

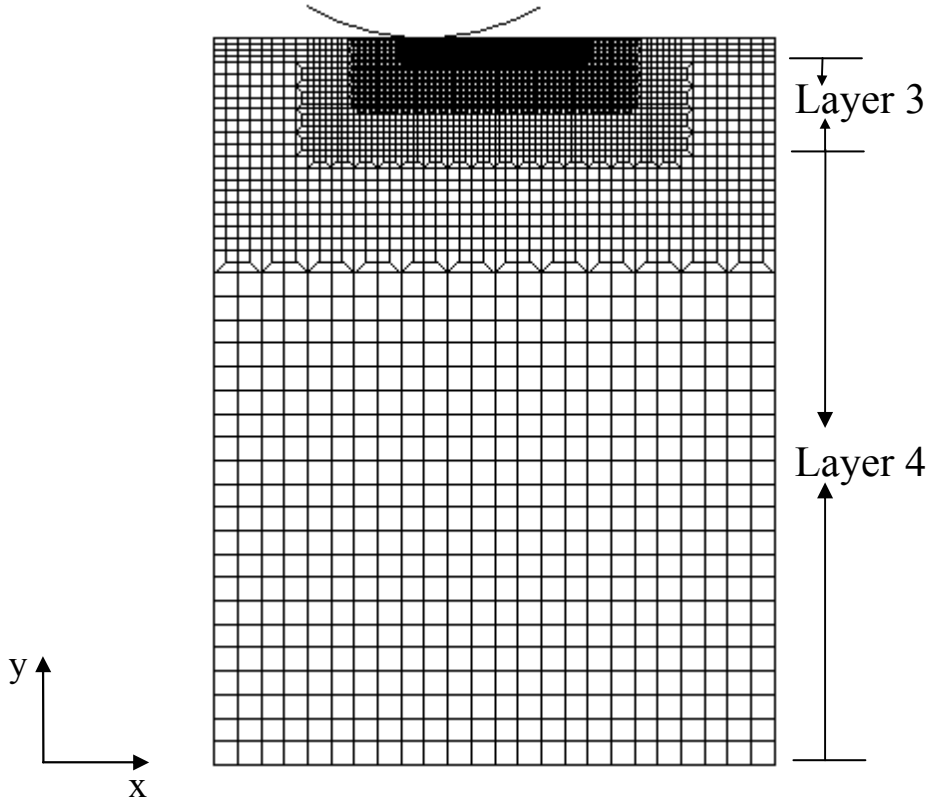

(b)

Figure 2

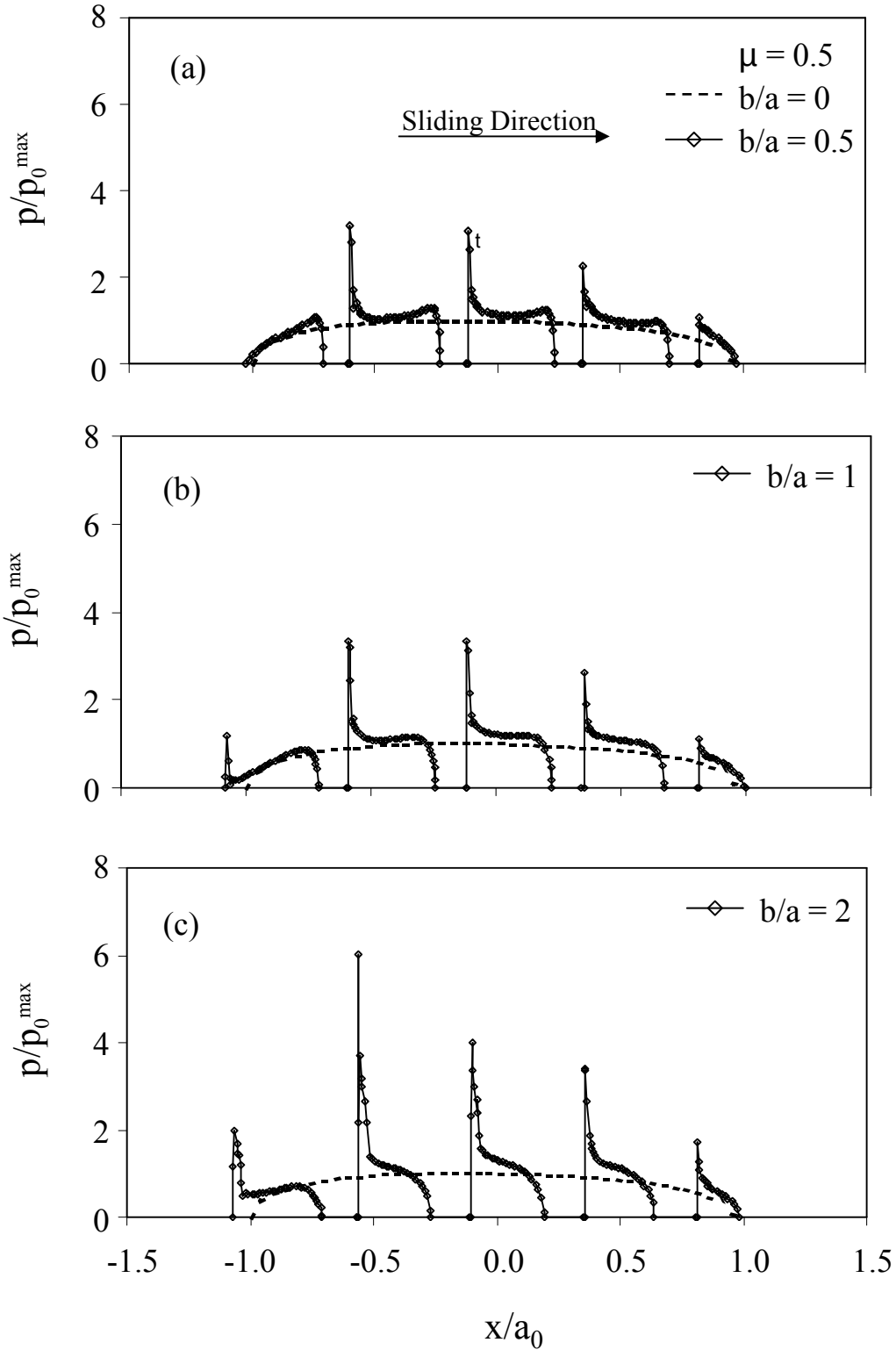
(a)
μ = 0.5
b/a = 0
b/a = 0.5
Sliding Direction
t
(b)
b/a = 1
(c)
b/a = 2
p/p0max
x/a0
0
2
4
6
8
-1.5
-1.0
-0.5
0.0
0.5
1.0
1.5

Figure 3

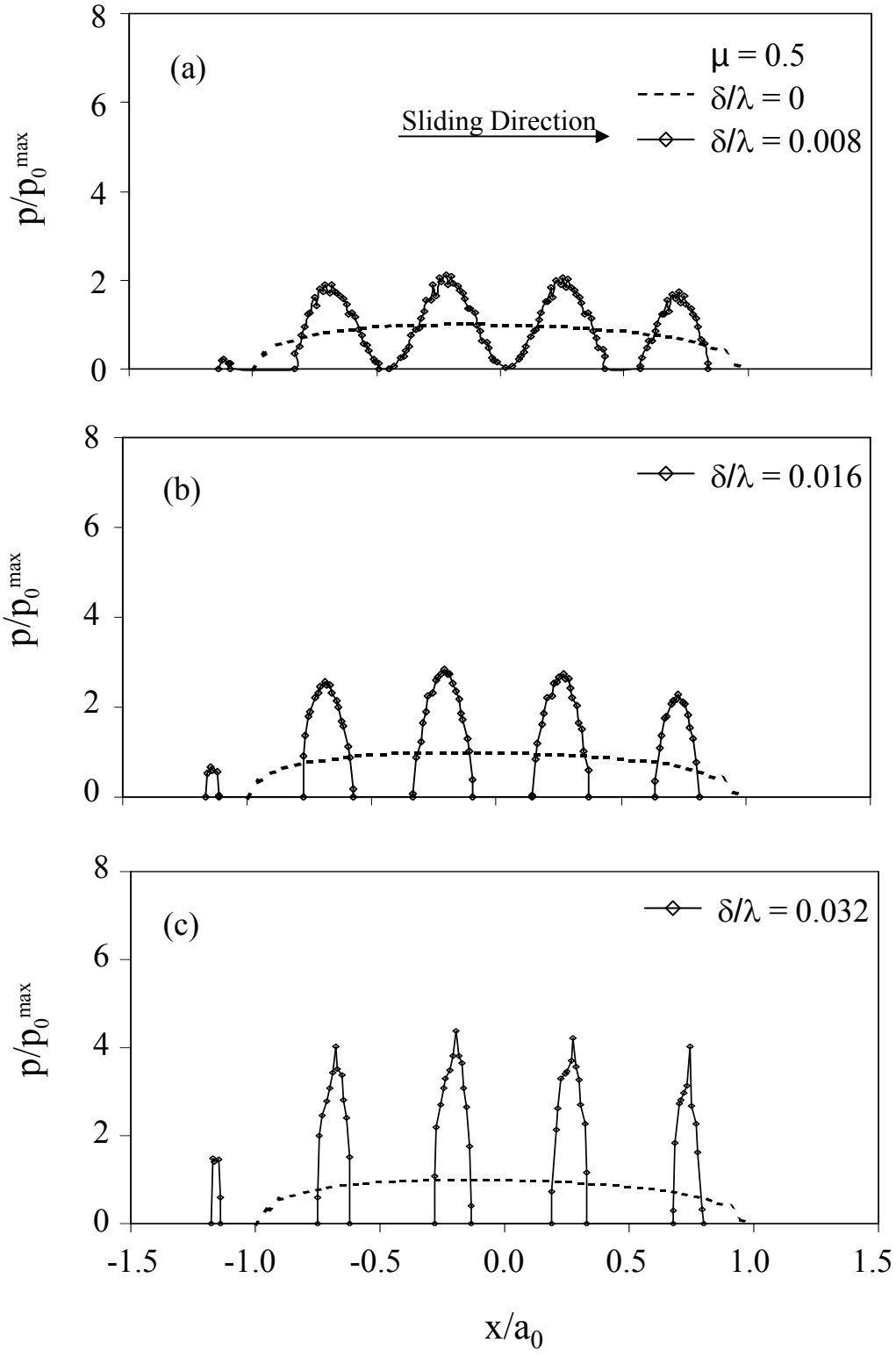
(a)
μ = 0.5
δ/λ = 0
δ/λ = 0.008
Sliding Direction
(b)
δ/λ = 0.016
(c)
δ/λ = 0.032
p/p0max
x/a0
0
2
4
6
8
-1.5
-1.0
-0.5
0.0
0.5
1.0
1.5

Figure 4

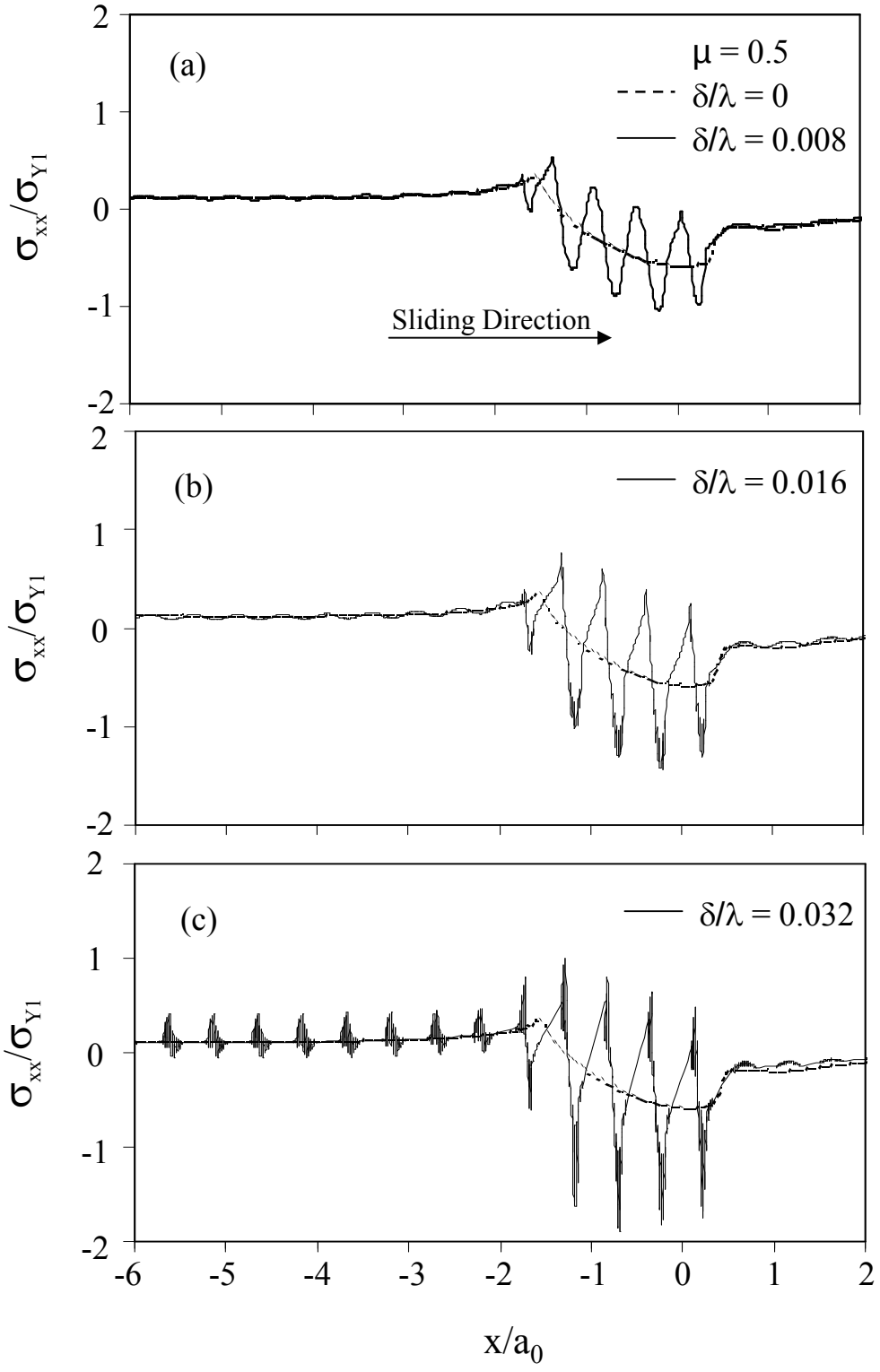
(a)
μ = 0.5
δ/λ = 0
δ/λ = 0.008
Sliding Direction
(b)
δ/λ = 0.016
(c)
δ/λ = 0.032
σxx/σY1
x/a0
2
1
0
-1
-2
-6
-5
-4
-3
-2
-1
0
1
2

Figure 5

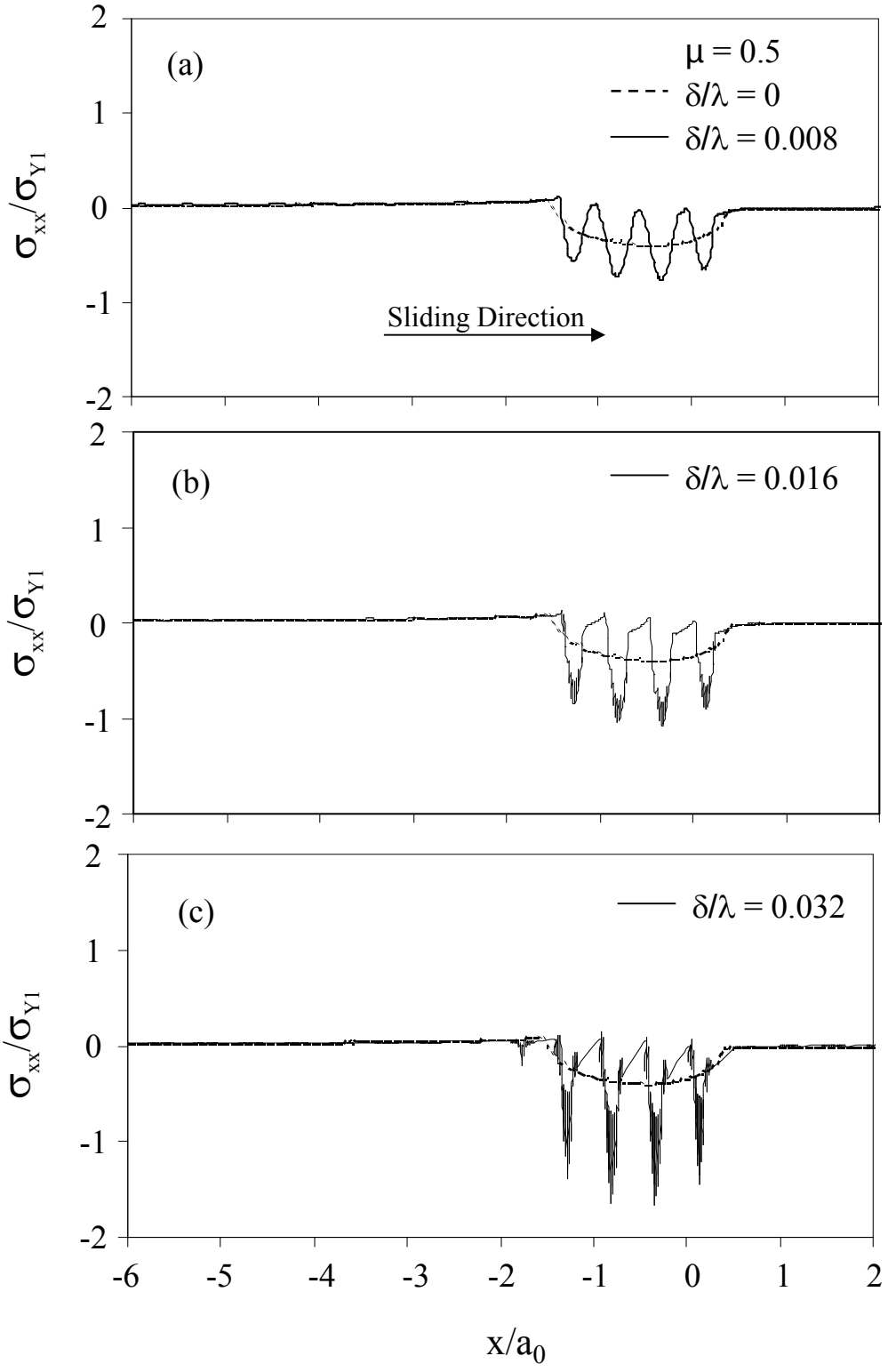
(a)
μ = 0.5
δ/λ = 0
δ/λ = 0.008
Sliding Direction
(b)
δ/λ = 0.016
(c)
δ/λ = 0.032
σxx/σY1
x/a0
2
1
0
-1
-2
-6
-5
-4
-3
-2
-1
0
1
2

Figure 6

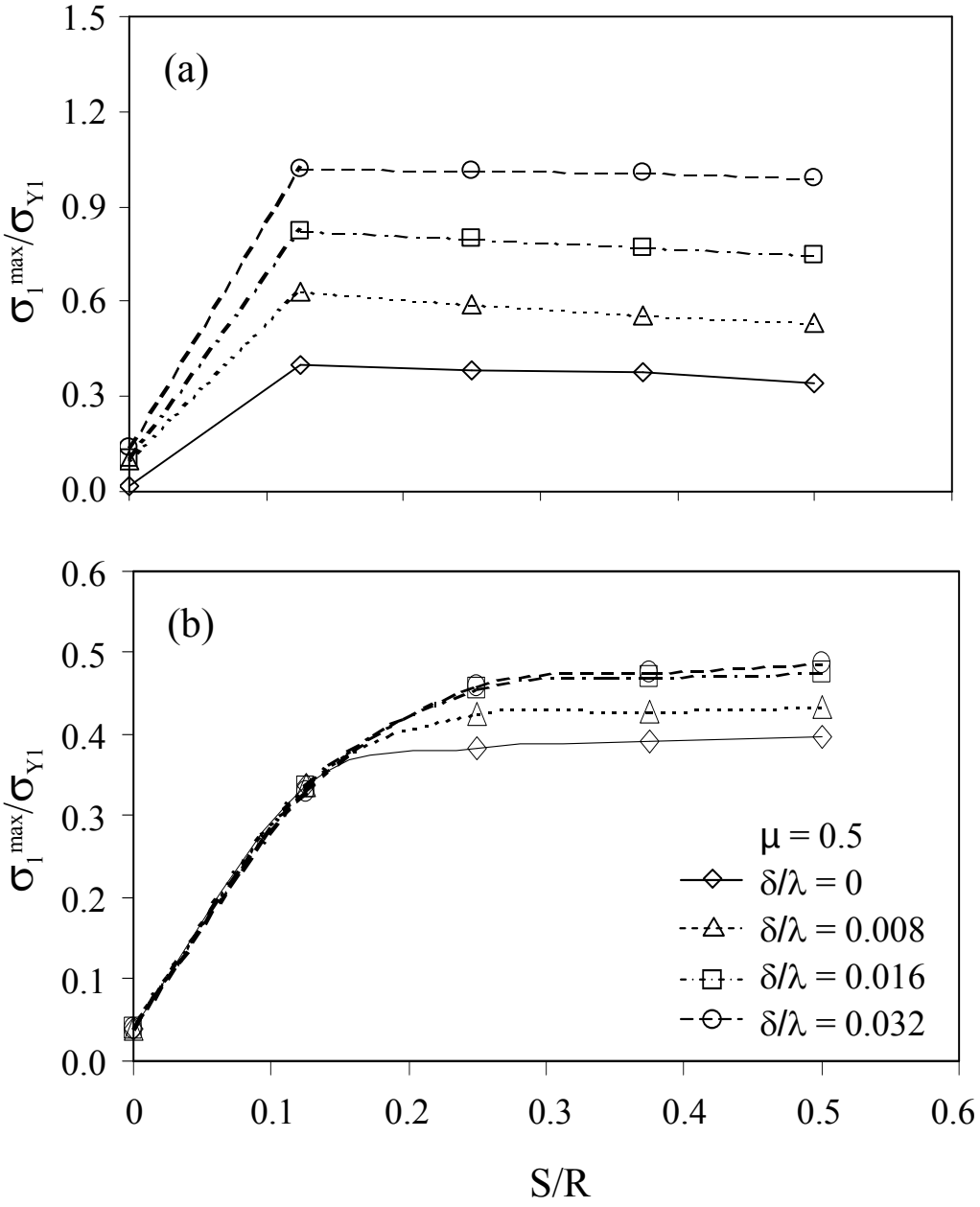

Figure 7

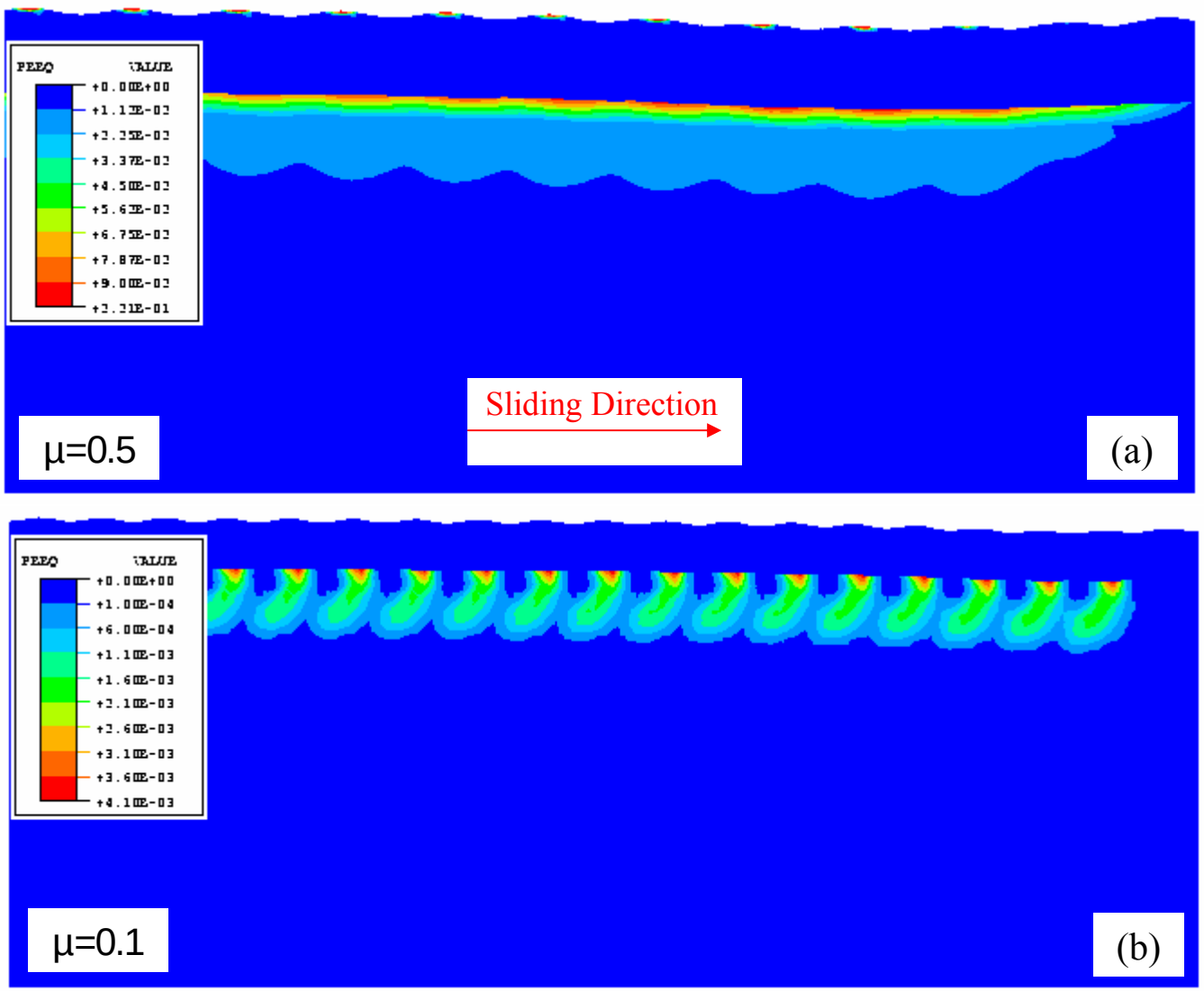
PEEQ
VALUE
+0.00E+00
+1.12E-02
+2.25E-02
+3.37E-02
+4.50E-02
+5.62E-02
+6.75E-02
+7.87E-02
+9.00E-02
+2.21E-01
Sliding Direction
μ=0.5
(a)
PEEQ
VALUE
+0.00E+00
+1.00E-04
+6.00E-04
+1.10E-03
+1.60E-03
+2.10E-03
+2.60E-03
+3.10E-03
+3.60E-03
+4.10E-03
μ=0.1
(b)

Figure 8

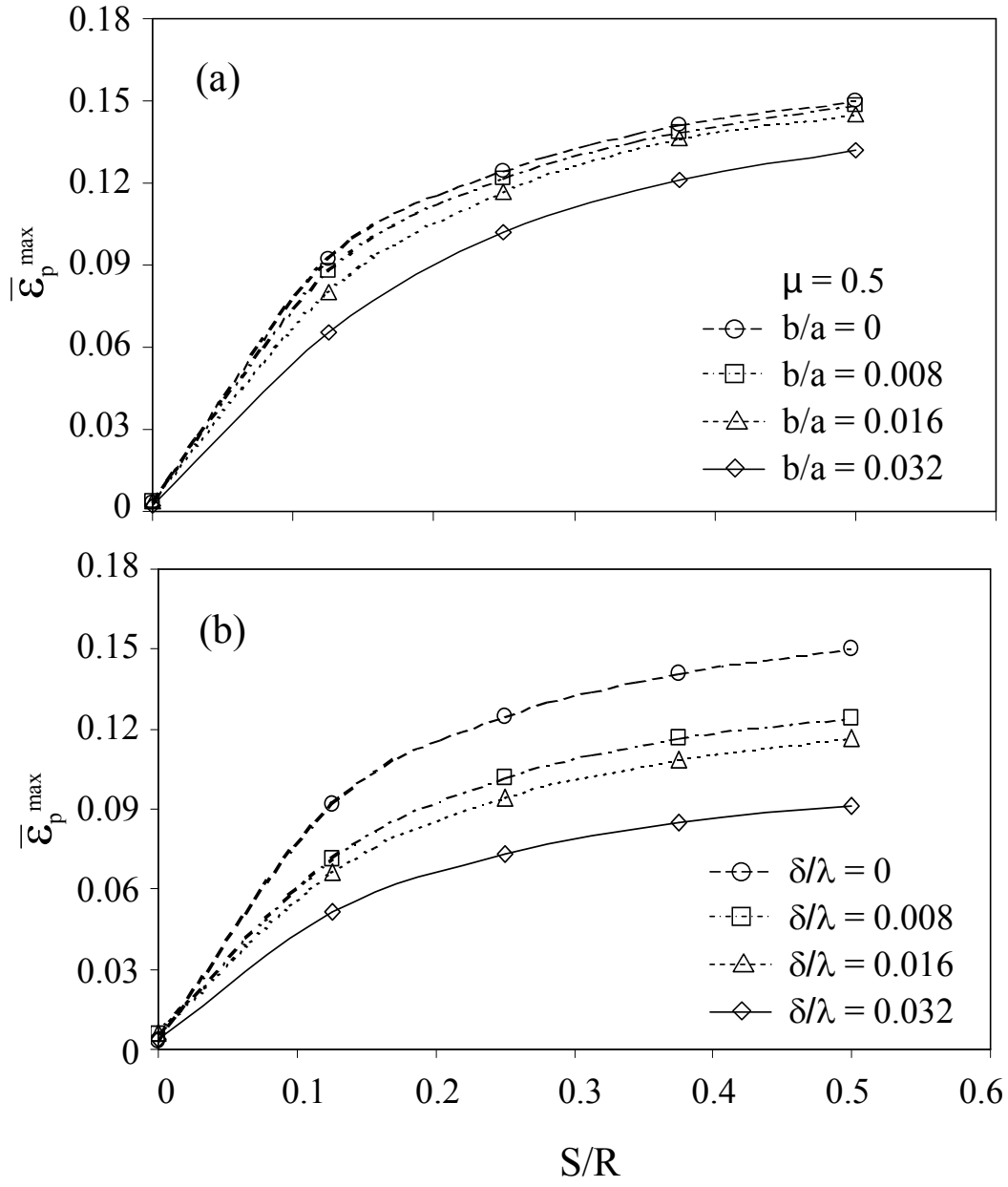
(a)
μ = 0.5
b/a = 0
b/a = 0.008
b/a = 0.016
b/a = 0.032
(b)
δ/λ = 0
δ/λ = 0.008
δ/λ = 0.016
δ/λ = 0.032
$\overline{\varepsilon}_p^{max}$
0.18
0.15
0.12
0.09
0.06
0.03
0
0.1
0.2
0.3
0.4
0.5
0.6
S/R

Figure 9

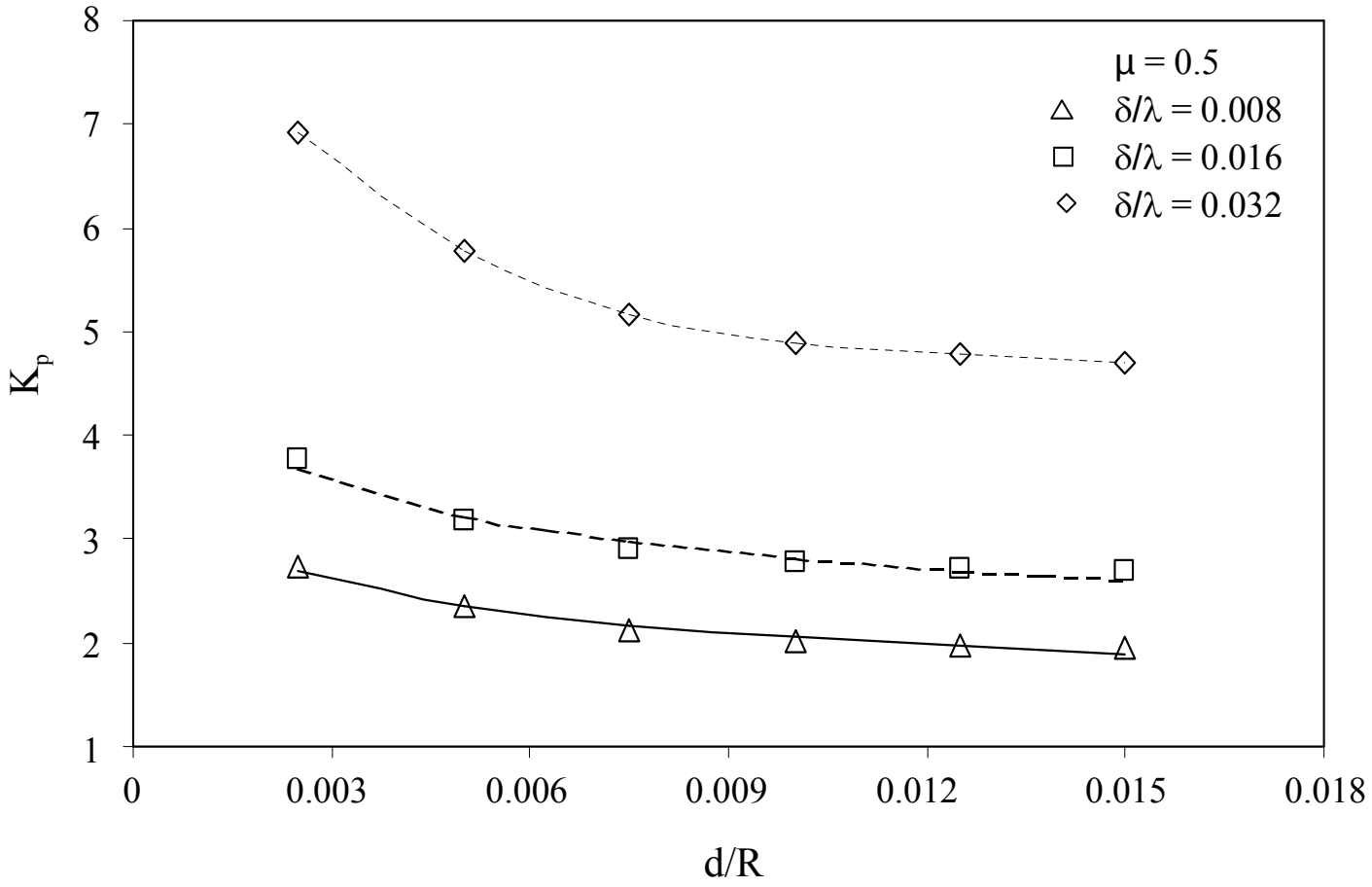
8
7
6
5
4
3
2
1
K_p
0
0.003
0.006
0.009
0.012
0.015
0.018
d/R
μ = 0.5
δ/λ = 0.008
δ/λ = 0.016
δ/λ = 0.032

Figure 10

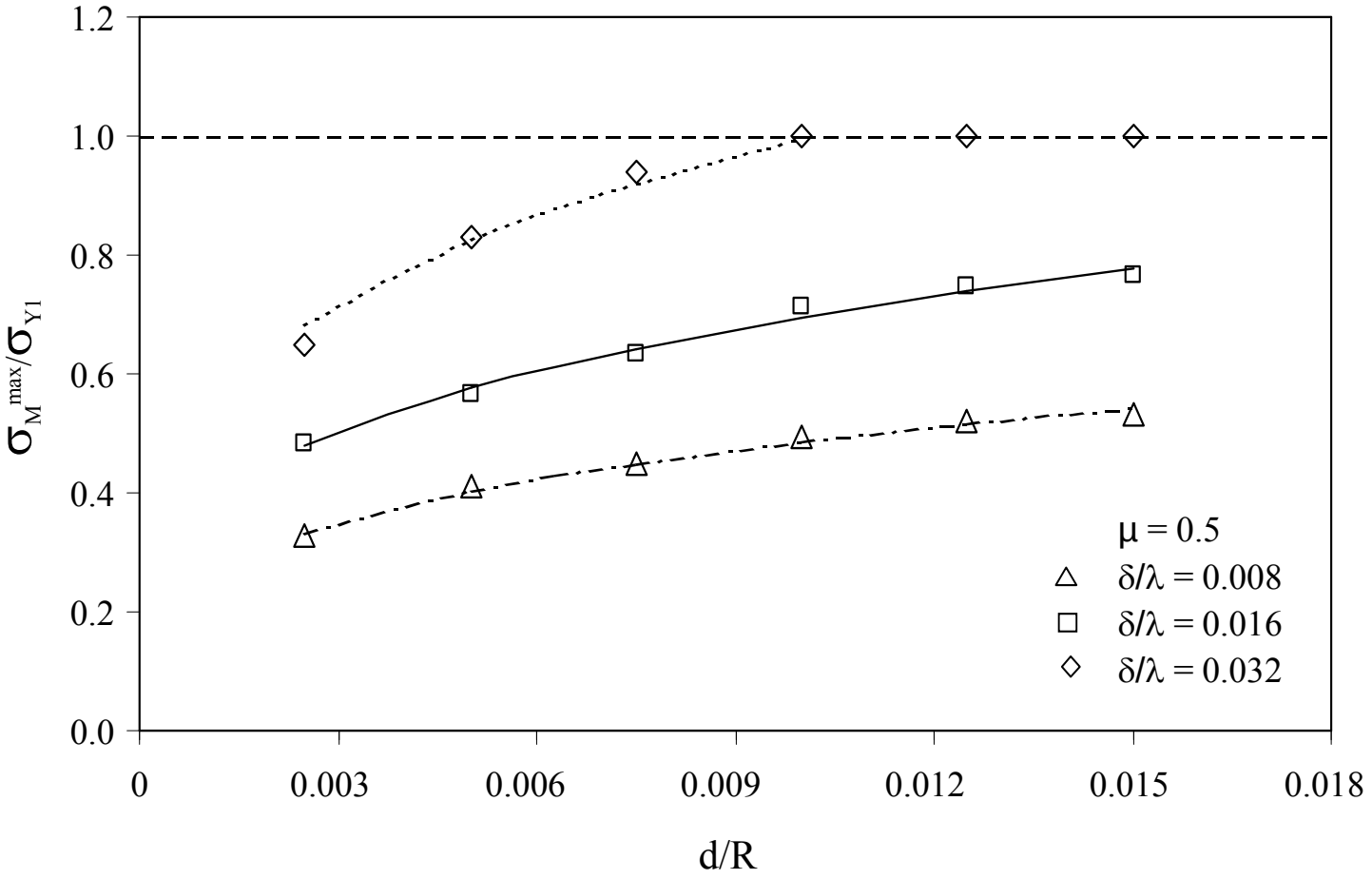
1.2
1.0
0.8
0.6
0.4
0.2
0.0
$\sigma_M^{max}/\sigma_{Y1}$
0
0.003
0.006
0.009
0.012
0.015
0.018
d/R
μ = 0.5
δ/λ = 0.008
δ/λ = 0.016
δ/λ = 0.032

Figure 11

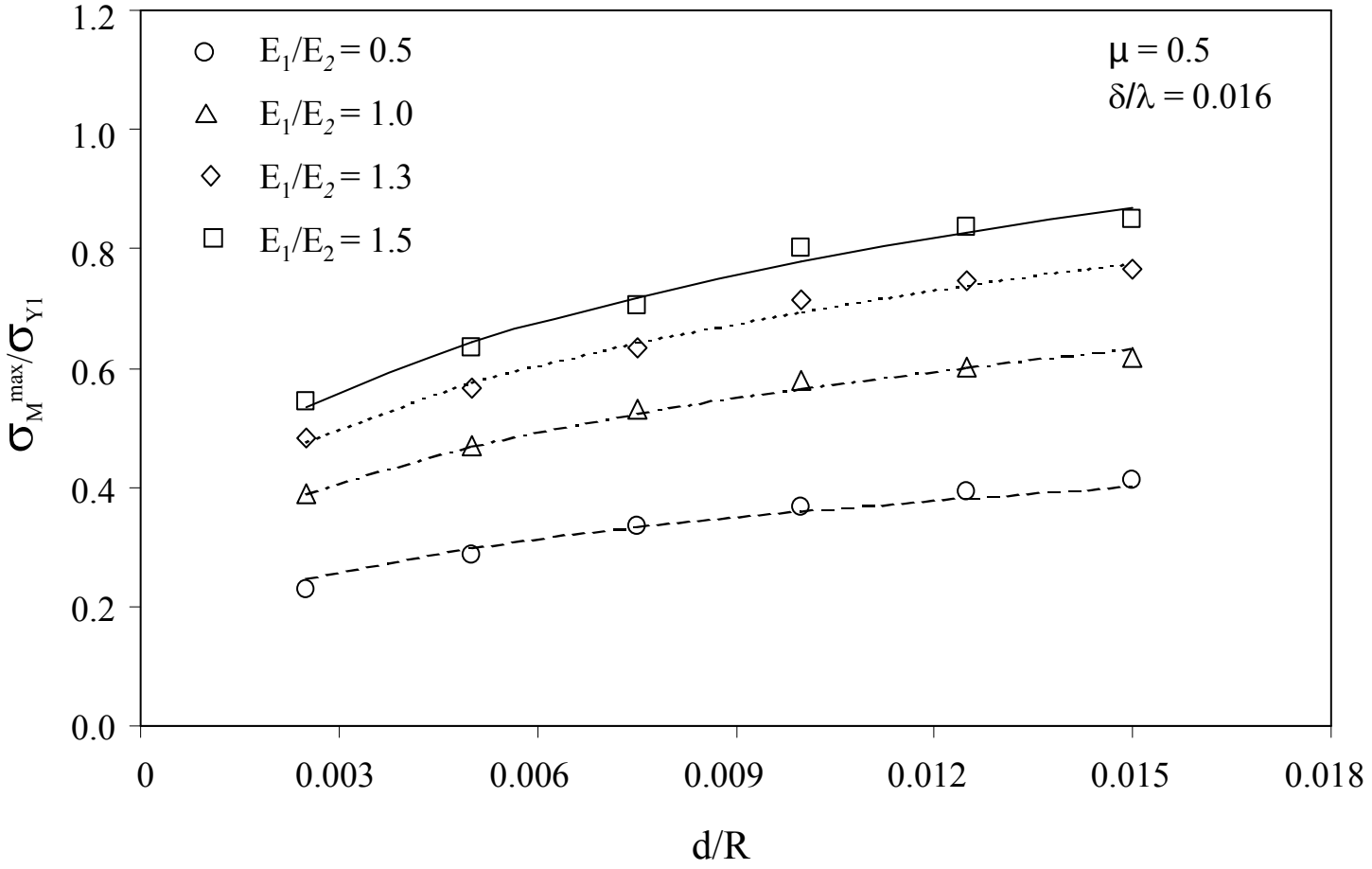
1.2
1.0
0.8
0.6
0.4
0.2
0.0
0
0.003
0.006
0.009
0.012
0.015
0.018
d/R
$\sigma_M^{max}/\sigma_{Y1}$
$E_1/E_2 = 0.5$
$E_1/E_2 = 1.0$
$E_1/E_2 = 1.3$
$E_1/E_2 = 1.5$
$\mu = 0.5$
$\delta/\lambda = 0.016$

Figure 12

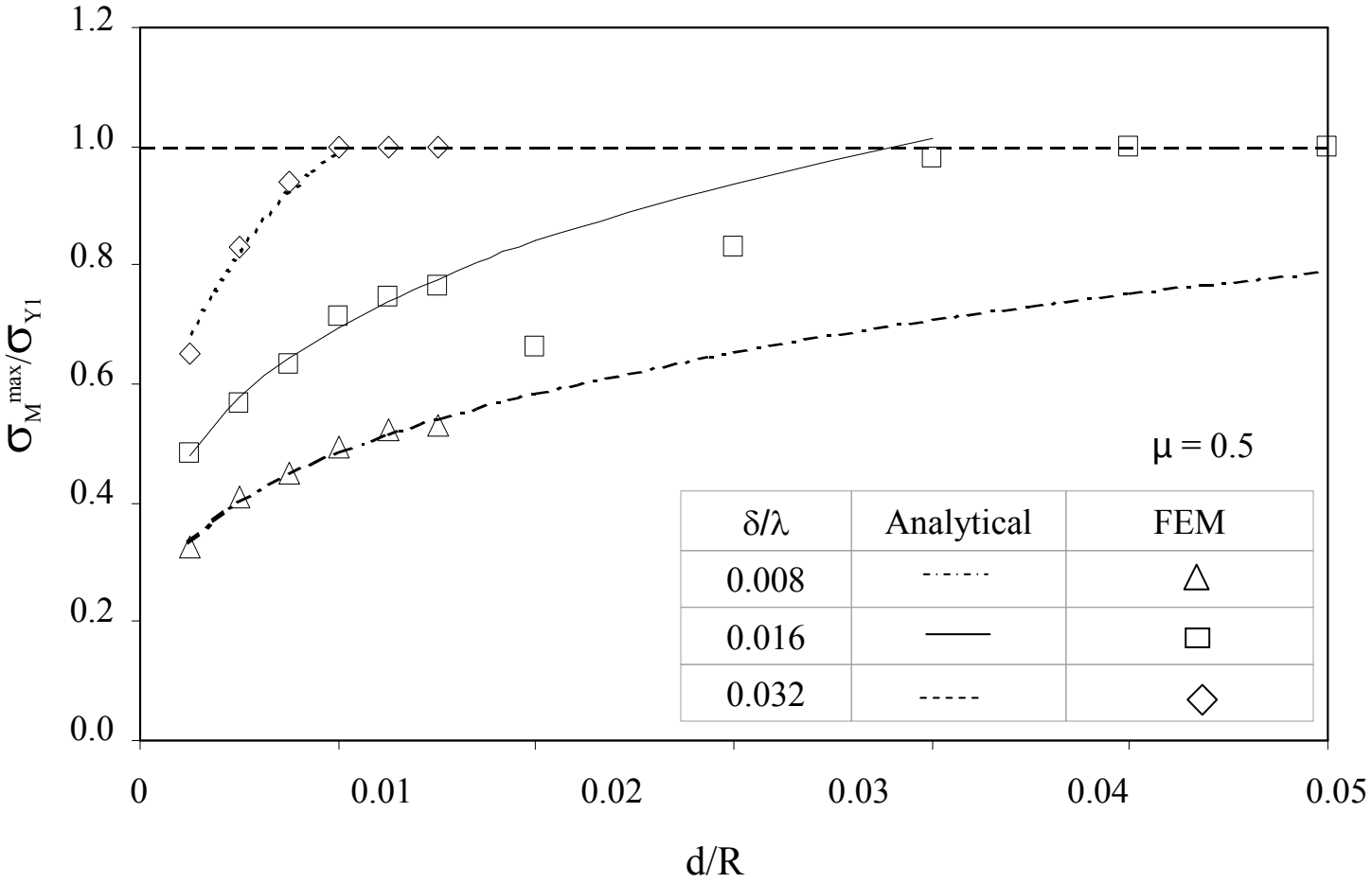
1.2
1.0
0.8
0.6
0.4
0.2
0.0
$\sigma_M^{max}/\sigma_{Y1}$
0
0.01
0.02
0.03
0.04
0.05
d/R
μ = 0.5
δ/λ
Analytical
FEM
0.008
0.016
0.032

Figure 13